International Journal of Multiphase Flow 168 (2023) 104566

Contents lists available at ScienceDirect

International Journal of Multiphase Flow

journal homepage: www.elsevier.com/locate/ijmulflow

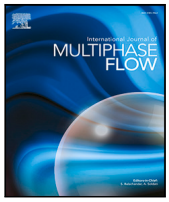

High-fidelity simulations of a rotary bell atomizer with electrohydrodynamic effects

Venkata Krisshna [a,*], Wanjiao Liu [b], Mark Owkes [a]

[a] Montana State University, Department of Mechanical & Industrial Engineering, P.O. Box 173800, Bozeman, MT 59717-3800, USA
[b] Ford Motor Company, Research and Innovation Center, 2101 Village Road, Dearborn, MI 48121, USA

ARTICLE INFO

Keywords:
NGA
CFD
Electric field
Charge distribution
Electrospray
Rotary atomizer

ABSTRACT

Electrostatic rotary bell atomizers are extensively used as paint applicators in the automobile industry. Paint undergoes atomization after exiting the edge of a high-speed rotating bell. In most setups, the paint is electrically charged and a background electric field is applied between the nozzle and the target surface to increase the transfer efficiency (TE). The atomization process directly determines the droplet size and droplet charge distributions which subsequently control TE and surface finish quality. Optimal spray parameters used in industry are often obtained from expensive trial-and-error methods. In this work, three-dimensional near-bell atomization is computationally simulated using a high-fidelity volume-of-fluid transport scheme that includes electrohydrodynamic (EHD) effects. We find that electrifying the setup results in the production of smaller droplets. Additionally, the electric field has a minor effect on primary atomization but a negligible effect on the size and stability of atomized droplets after secondary breakup. This cost-effective method of simulating EHD-assisted atomization allows for the understanding of the effect of the electric field and the extraction of droplet charge characteristics which is otherwise challenging to obtain experimentally.

1. Introduction

With the world becoming increasingly dependent on automotive means of transportation and motor vehicle production approaching 100 million units per year (OICA, 2019), automobile manufacturers are looking for ways to minimize production costs. In an automobile manufacturing facility, the paint shop can account for up to 70% of the total energy costs (Galitsky and Worrel, 2008), demand up to 50% of the electricity and up to 60% of the fossil fuel energy (Leven and Weber, 2001) used in the facility. These costs are associated with the energy used in operating and maintaining the HVAC equipment of the painting booth, paint drying, and control of pollutants like volatile organic compounds generated by paint overspray (Galitsky and Worrel, 2008). The overspray leads to significant material waste causing environmental and cost concerns. The paint shop is thus one of the most expensive aspects of automobile manufacturing, accounting for up to 50% of its total costs (Akafuah et al., 2013; Clément et al., 2014). The global automotive paints and coatings market size was valued at $17.34 bn in 2019 and is expected to be about $26.8 bn by 2027 (Precedence Research, 2019). Additionally, the paint shop is responsible for over 80% of the environmental concerns in a manufacturing facility (Geffen and Rothenberg, 2000).

Rotary bell atomizers (RBAs) (Fig. 1) are extensively used as paint applicators in the automobile industry. In addition to automobile paint shops, rotary atomizers are used in several other applications such as agricultural spraying (Craig et al., 2014), food processing (Oxley, 2012), and pharmaceutical drug-delivery (Mackaplow et al., 2006).

An RBA is a high-speed rotating nozzle that atomizes paint into droplets that range from a few micrometers to tens of micrometers in diameter. Paint is injected onto the inner surface of a bell-shaped nozzle where it spreads into a thin film on the surface due to centrifugal forces. The fluid film, on reaching the edge of the high-speed rotating bell, exits as multiple ligaments which further atomize into droplets (Frost, 1981). It is common practice to electrically charge the paint and apply a background electric field to enhance the transfer efficiency (TE) of the device (Domnick and Thieme, 2006; Im et al., 2000). Atomized droplets, which also carry electric charge, move towards the grounded target surface under the influence of the electric field.

Metrics of significant importance such as the droplet size uniformity, surface finish quality, TE, deposition thickness, and environmental impact are directly dependent on the atomization process in the nozzles (Domnick and Thieme, 2006; Akafuah et al., 2016; Corbeels et al., 1992). The nozzle operating conditions used in industry

* Corresponding author.
E-mail addresses: venkat.krisshna@student.montana.edu (V. Krisshna), lwanjiao@ford.com (W. Liu), mark.owkes@montana.edu (M. Owkes).

https://doi.org/10.1016/j.ijmultiphaseflow.2023.104566
Received 15 February 2023; Received in revised form 20 June 2023; Accepted 28 June 2023
Available online 5 July 2023

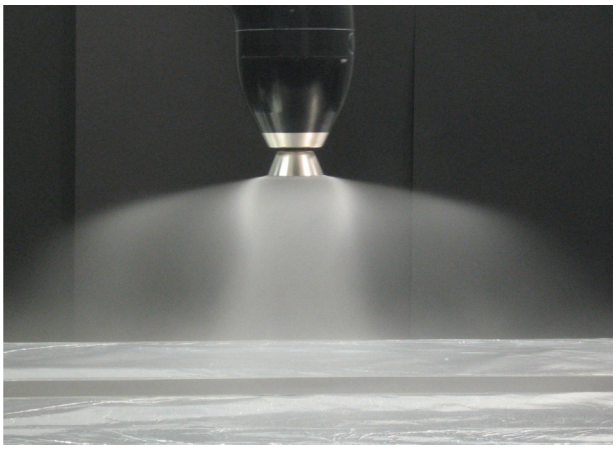

Fig. 1. A rotary bell atomizer in operation. Photograph courtesy of RISE Research Institutes of Sweden and Fraunhofer-Chalmers Centre.

that optimize these metrics are often obtained from expensive trial-and-error experimental methods. The optimal setup of RBAs can still be improved, for example, painters currently are required to overcoat the target surface to ensure sufficient finish quality using excess paint (Sadegh et al., 2018). Due to the high expense of the painting process, small improvements can result in significant cost savings and waste reduction.

Early research conducted in RBAs investigated the physics behind the atomization process (Hinze and Milborn, 1950; Balachandran and Bailey, 1984; Domnick, 2010; Mahmoud and Youssef, 2014; Naoki et al., 2019; Corbeels et al., 1992; Loch et al., 1998; Dombrowski and Lloyd, 1974). These works identified four crucial processes leading up to atomization — film formation, ligament formation, ligament thinning, and ligament breakup. Several articles have studied and characterized the process of film formation as paint flows along the inner surface of the bell (Tatsuya et al., 2015; Domnick et al., 2008; Kuhnhenn et al., 2018; Makarytchev et al., 1997; Symons and Bizard, 2015) and ligament formation at the edge of the bell (Rezayat and Farshchi, 2019; Shirota et al., 2012; Saye et al., 2023). In this work, ligament thinning and ligament breakup are the relevant physical processes. While many RBAs are equipped with shaping air (an annular stream of focused air around the bell) to increase TE, the system modeled here does not include it.

Multiple research groups have studied the operation of non-electrified RBAs focusing on various aspects such as the bell geometry (Domnick, 2010; Sidawi et al., 2021a; Kazama, 2003; Panneton, 2002), the effect of shaping air (Stevenin et al., 2015; Darwish Ahmad et al., 2018), the breakup process (Shen et al., 2019; Ogasawara et al., 2010; Keshavarz et al., 2020; Saye et al., 2023), and the droplet size distribution (Ahmad et al., 2019).

As mentioned, RBAs are often operated in a background electric field that helps improve their TE. The electric field interacts with the charged liquid and affects its flow near the bell. Electrified flows are described by electrohydrodynamics (EHD) - the science of characterizing interactions between fluid dynamics and electrostatics (Chen et al., 2003; Fylladitakis et al., 2014). EHD has seen several decades of research and is now employed in various engineering applications including food technology (Anukiruthika et al., 2021; Khan et al., 2012; Gorty and Barringer, 2011), inkjet printing (Raje and Murmu, 2014), electrostatic precipitation (Yamamoto and Velkoff, 1981), powder coating (Jaworek et al., 2018), biochemistry (Stimpson and Evans Jr., 1978), microfluidics (Azizian et al., 2019), and biomedical applications (Enayati et al., 2011; Eagles et al., 2006; Farook et al., 2007). It is common practice to use electric fields to control uncharged liquid jets (Vajdi Hokmabad et al., 2014) and charged fuel sprays (Fredrich et al., 2022; Shrimpton and Laoonual, 2006). EHD-assisted atomization has been an increasingly important means of producing liquid droplets that is well-established to offer advantages over other industrial spraying processes (Bailey, 1974; Hayati et al., 1986; Grace and Marijnissen, 1994).

Previous studies on electrified RBAs that have included an electrostatic model have explored its effects as a macroscopic phenomenon focusing on the resulting spray pattern, paint film thickness, over-spray control, and TE (Arumugham-Achari et al., 2015; Im et al., 2004; Domnick et al., 2005; Colbert and Cairncross, 2005; Ellwood and Braslaw, 1998; Sidawi et al., 2021b; Pendar and Páscoa, 2021; Mark et al., 2013; Im et al., 2003, 2000; Hines, 1966; Viti et al., 2010). Experimental studies on near-bell atomization in electrified RBAs have been limited in their ability to understand droplet charge characteristics (Wilson et al., 2018). Recent numerical efforts have characterized the effects of various operating parameters on droplet trajectories, droplet size distribution, and charge evaporation in electrified RBAs (Colbert, 2007; Ellwood et al., 2014; Pendar and Páscoa, 2019, 2020; Ray and Henshaw, 2018; Guettler et al., 2020). Generally, most prior models have given little or no attention to electric effects on multiphase transport phenomena driving atomization. Moreover, high-speed cameras and imaging equipment are seldom placed in electrified RBA setups to prevent electric arcing (Gödeke et al., 2021). For these reasons, experimental studies of the atomization process in electrified RBAs are limited in detail. Additionally, there is currently no experimental data on the charge distribution in atomized droplets in RBAs. Although some research has been conducted on the effect of charge density on the surface finish quality (Toljic et al., 2011) and charge distribution in atomized droplets (McCarthy and Senser, 2005) in electrostatic sprays, they have not been studied for charged rotary atomizers.

The process of atomization in the presence of an electric field can be modeled using the incompressible Navier–Stokes and EHD governing equations. In this way, the operation of this device can be studied computationally for a wide range of parameters without the cost of operating the device in a lab. Moreover, numerical analysis allows varying fluid properties with ease thus avoiding the expensive process of meticulously fabricating an appropriate fluid for experimental procedures.

In this project, we investigate the microscopic effects of EHD on atomization by computationally simulating three-dimensional RBA near-bell atomization using a high-fidelity volume-of-fluid transport scheme that includes EHD effects. We perform numerical experiments to understand the effect of EHD on atomization to obtain and examine the resulting droplet size distributions and droplet charge distributions in the atomized droplet cloud near the nozzle. Ultimately, this research contributes to the understanding of the underlying physics in electrically-assisted atomization processes and provides insight into the droplet conditions after atomization. These conditions can serve as initial conditions for a Lagrangian flow solver that predicts the trajectories of the atomized charged droplets towards the target surface in a background electric field.

The governing equations of the physics modules used to model liquid flows in electrified RBAs are detailed in Section 2. The validation efforts of the physics modules, details of the domain geometry, and the mesh sensitivity of the tool are presented in Section 3. Inferences from a parameter study and atomization statistics are addressed in Section 4. Section 5 contains a summary of the project and potential future work that can be conducted with the tool built to study atomization in electrified RBAs.

2. Governing equations

The physics modules discussed below have been implemented within a code called NGA - a high-order, fully conservative, variable density, low Mach number Navier–Stokes solver that contains various

multi-physics modules implemented in parallel using message passing interface (MPI). The formulation discretely conserves mass and momentum in a periodic domain. NGA uses a conservative unsplit geometric volume-of-fluid (VOF) scheme as described in the works of Blanquart et al. (2009), Desjardins et al. (2008a,b) and Owkes and Desjardins (2015b,a, 2014, 2017). NGA has been developed by several groups to solve multiphase EHD flows, details of which can be found in Van Poppel et al. (2010) and Sheehy and Owkes (2017).

2.1. Multiphase fluid dynamics

For low-Mach number, variable density, multiphase flows, mass and momentum conservation laws in both phases can be written as follows

$$\frac{\partial \rho_i}{\partial t} + \nabla \cdot (\rho_i \mathbf{u}_i) = 0 \tag{1}$$

$$\frac{\partial \rho_i \mathbf{u}_i}{\partial t} + \nabla \cdot (\rho_i \mathbf{u}_i \otimes \mathbf{u}_i) = -\nabla p_i + \nabla \cdot (\boldsymbol{\sigma}_i^{\mathrm{f}} + \boldsymbol{\sigma}_i^{\mathrm{e}}) + \gamma \kappa \mathbf{n} \delta_s + \mathbf{f}_{\mathrm{external}} \tag{2}$$

where ρ is the density, $\mathbf{u}$ is the velocity field vector, t is time, and p is the hydrodynamic pressure. The subscript i denotes the fluid phase (gas or liquid). The term $\gamma \kappa \mathbf{n} \delta_s$ denotes surface tension force, where γ is the surface tension coefficient, κ is the local curvature of the interface computed using the ACES technique (Owkes et al., 2018), $\mathbf{n}$ is the normal vector to the interface, and δ_s is a Dirac-delta function that is nonzero only on the interface (Owkes and Desjardins, 2015b). The viscous stress tensor $\boldsymbol{\sigma}_i^{\mathrm{f}}$ in Eq. (2) is given by

$$\boldsymbol{\sigma}_i^{\mathrm{f}} = \mu_i (\nabla \mathbf{u}_i + \nabla \mathbf{u}_i^{\mathrm{T}}) - \frac{2}{3} \mu_i (\nabla \cdot \mathbf{u}_i) \mathbb{I} \tag{3}$$

where μ is the dynamic viscosity and $\mathbb{I}$ is the identity tensor. These equations form the basis of the fluid dynamics module in this work and further details can be found in Owkes and Desjardins (2017, 2014) and Desjardins et al. (2008a,b). $\boldsymbol{\sigma}_i^{\mathrm{e}}$ is the Maxwell stress tensor which will be described in the next section. $\mathbf{f}_{\mathrm{external}}$ is a combination of the forces experienced by a fluid element in the system.

$$\mathbf{f}_{\mathrm{external}} = \mathbf{f}_{\mathrm{centrifugal}} + \mathbf{f}_{\mathrm{Coriolis}} + \mathbf{f}_{\mathrm{gravity}} \tag{4}$$

2.2. Electrohydrodynamics

The Maxwell stress tensor $\boldsymbol{\sigma}_i^{\mathrm{e}}$ in Eq. (2) is given by

$$\boldsymbol{\sigma}_i^{\mathrm{e}} = \varepsilon_i \mathbf{E}_i \otimes \mathbf{E}_i - \frac{\varepsilon_i}{2} \mathbf{E}_i \cdot \mathbf{E}_i \left(1 - \frac{\rho_i}{\varepsilon_i} \frac{\partial \varepsilon_i}{\partial \rho_i}\right) \mathbb{I} \tag{5}$$

where $\mathbf{E}$ is the electric field vector and ε is the electric permittivity equal to the product of the relative permittivity κ_i and the vacuum permittivity space ε_0. Magnetic effects have been ignored since the EHD time scale is several orders of magnitude larger than the magnetic time scale (Saville, 1997) in the atomization process that is of interest here. This electrostatic assumption eliminates the effect of the velocity of the charges (i.e., current) on the electric field thus dictating that the electric field is only influenced by the instantaneous electric charge distribution. The electric force can be expressed as the divergence of the Maxwell stress tensor,

$$\nabla \cdot \boldsymbol{\sigma}_i^{\mathrm{e}} = q_i \mathbf{E}_i - \frac{1}{2} \mathbf{E}_i^2 \nabla \varepsilon_i + \nabla \left(\frac{1}{2} \rho_i \frac{\partial \varepsilon_i}{\partial \rho_i} \mathbf{E}_i^2 \right) \tag{6}$$

where q is the volumetric electric charge density. The first term on the right-hand side of Eq. (6) is the Coulomb (or Lorentz) force. The second and third terms denote the dielectric and the electrostrictive forces respectively, which are only significant in a transient electric field with time scales several orders of magnitude larger than what is encountered in atomization problems (Kourmatzis and Shrimpton, 2009).

As the electric field vector is irrotational it can be expressed in terms of the scalar electric potential ϕ as

$$\mathbf{E}_i = -\nabla \phi. \tag{7}$$

The electric potential Poisson equation describes the relationship between charge density q_i and ϕ as

$$-\nabla \cdot (\varepsilon_i \nabla \phi) = q_i. \tag{8}$$

The electric Poisson equation is solved using the hypre library of routines for scalable parallel solutions of linear systems (Falgout et al., 2004, 2006).

The accumulation of bulk volumetric charge as a surface charge in a thin electric boundary layer much smaller than the hydrodynamic boundary layer is a commonly made assumption in charged jet simulations (Wang et al., 2019; Turnbull, 1989). The electric charge has previously been modeled in two ways: either a constant bulk volumetric charge or a fully relaxed surface charge. According to the classic leaky dielectric model (Melcher and Taylor, 1969; Taylor, 1966; Saville, 1997) that is commonly used to describe the effects of electric charge in dielectric liquids, the fundamental underlying assumption is that bulk volumetric electric charge has sufficient time to fully relax to a surface charge. However, for atomizing flows the advection time scale is similar to the charge relaxation time scale and a fully relaxed charge assumption is invalid. The charge relaxation time τ_q represents the time required for volumetric charge q_l to relax to the surface (Crowley, 1986; Kourmatzis and Shrimpton, 2009). The fluid advection timescale τ_f is a characteristic time for a fluid element to move across a relevant length scale L_0. The ratio of the two time scales called the electric Reynolds number Re_e was formulated in Stuetzer (1962) as

$$\tau_q = \frac{\varepsilon_l}{\psi_l \, q_l}, \tag{9}$$

$$\tau_f = \frac{L_0}{\mathbf{u}}, \tag{10}$$

$$\mathrm{Re}_e = \frac{\tau_q}{\tau_f} \tag{11}$$

where values of the quantities that correspond to typical automotive paints and RBA operations listed in Table 1 yield a value of Re_e approximately equal to 8.93. This suggests that the advection and charge relaxation timescales are comparable in this application. The above time scale analysis highlights the necessity to model the process of charge relaxation by migration and diffusion in addition to advection with the fluid velocity. The common assumption of charges to be accumulated on the surface disallows the charge migration dynamics and limits the accuracy of the droplet charge distribution after atomization. In this work, we assume a constant bulk volumetric charge at the injector and allow charges to relax as the jet propagates through the domain. Charge transport is described by the conservation equation

$$\frac{\partial q_i}{\partial t} + \nabla \cdot \mathbf{J}_i = 0 \tag{12}$$

where the current density $\mathbf{J}_i$ is formulated as (Melcher, 1981; Van Poppel et al., 2010)

$$\mathbf{J}_i = q_i \mathbf{u}_i + q_i \psi_i \mathbf{E}_i - \mathcal{D}_i \nabla q_i \tag{13}$$

where ψ_i is the charge mobility coefficient and $\mathcal{D}_i$ is the molecular diffusivity. The three terms that contribute to the current density can be described as advection due to the velocity field, advection due to the electrical velocity, and diffusion. In summary, the charge density field (q) and boundary conditions (BCs) in electric potential are used to obtain the electric potential field (ϕ) using Eq. (8). The electric field ($\mathbf{E}$) is then obtained using Eq. (7) after which Eq. (6) allows for the calculation of the Coulomb force ($\mathbf{f}_{\mathrm{electric}}$) on the charged fluid. More details on the equations involved in the formulation of the EHD module can be found in Sheehy and Owkes (2017).

2.3. Rotating reference frame

In an RBA undergoing ligament breakup mode, each ligament exiting the serrated bell edge behaves similarly with statistically similar droplet size distribution and charge transport behavior. Therefore, we

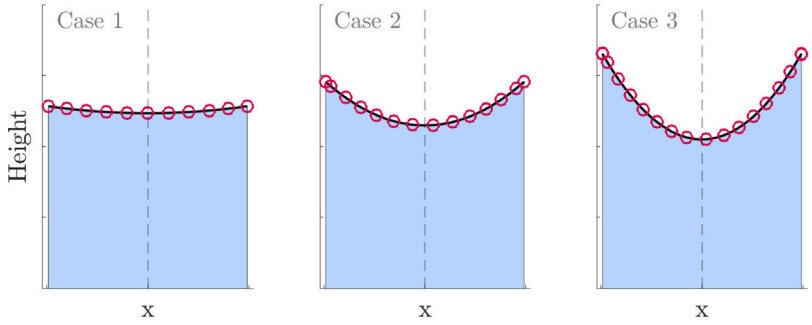

Fig. 2. Validation of centrifugal force: Numerical results of a rotating tank experiment where cases 1, 2, and 3 correspond to rotation rates of 4, 10, and 14 rad/s respectively. The analytical solution of the interface (Eq. (16)) at various locations is plotted with red circles. The numerically computed liquid interface and liquid bulk are shown as black lines and blue areas respectively. The dashed line represents the axis of rotation for each case. (For interpretation of the references to color in this figure legend, the reader is referred to the web version of this article.)

focus on one ligament ejected from the bell edge in our numerical simulations. We attach our reference frame to the rotating nozzle and ligament.

To account for the rotating nozzle and the consequent forces, we include equations that describe the rotating reference frame. This subjects the liquid to centrifugal and Coriolis forces which can be formulated as

$$\mathbf{f}_{\text{centrifugal}} = -\rho_i \boldsymbol{\omega} \times (\boldsymbol{\omega} \times \mathbf{r}) \tag{14}$$

$$\mathbf{f}_{\text{Coriolis}} = -2\rho_i \boldsymbol{\omega} \times \mathbf{u}_i \tag{15}$$

where $\boldsymbol{\omega}$ is the angular velocity and $\mathbf{r}$ is the radial distance from the axis of rotation.

3. Numerical simulations of RBA jets

3.1. Validation of physics modules

The EHD module in NGA has seen continued development and validation efforts have been presented in Sheehy and Owkes (2017).

To validate the implementation of centrifugal force (described in Section 2.3) into the EHD formulation, numerical experiments of a rotating tank configuration are conducted. The solution for the steady-state interface profile $h(x)$ of a liquid in a rotating tank is analytically derived as

$$h(x) = h_0 + \frac{1}{2g}(\boldsymbol{\omega} x)^2 \tag{16}$$

where h_0 is the height of the liquid at the axis of rotation and g is the gravitational acceleration (Laplace, 2009). Numerical results show excellent agreement with the analytical solution for varying rotation rates (Fig. 2). The numerical implementation of the Coriolis force (described in Section 2.3) is tested by simulating a liquid jet in a rotating frame. The path of an object experiencing the centrifugal and Coriolis forces follows a circle with a growing radius, i.e., a spiral. The analytical solution for the position of the object (x, y) at a given time t is obtained as

$$\begin{aligned} x(t) &= \left(x_0 + v_{x0}t\right)\cos(\boldsymbol{\omega}t) + t\left(v_{y0} + \boldsymbol{\omega}x_0\right)\sin(\boldsymbol{\omega}t) \\ y(t) &= -\left(x_0 + v_{x0}t\right)\sin(\boldsymbol{\omega}t) + t\left(v_{y0} + \boldsymbol{\omega}x_0\right)\cos(\boldsymbol{\omega}t) \end{aligned} \tag{17}$$

where v_{x0} and v_{y0} are the x and y components of the initial velocity of the jet and x_0 is the position of the jet at $t = 0$. The derivation of this analytical solution is provided in Appendix. This solution is derived for a rigid point-like object with its all mass concentrated at its center. Liquid jets, however, are not point-like approximations and include effects of viscosity and surface tension. Despite these challenges, we proceeded with validating the effect of the Coriolis force on liquid jets in a rotating reference frame and obtained satisfactory results. Numerically simulated liquid jets follow the analytically predicted trajectory for varying rotation rates (Fig. 3).

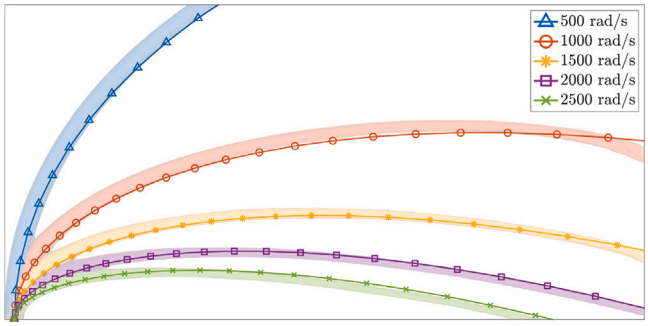

Fig. 3. Validation of Coriolis force: Numerical results of the liquid jet interfaces in a reference frame rotating counter-clockwise about an axis that points out of the 2D plane. The analytical solution (Eq. (17)) is shown as a superimposed solid line for each case.

3.2. Using e-Mesh

An addition to the EHD module of NGA developed for this project involves using a domain called e-Mesh. e-Mesh is much larger than the flow-solver domain (henceforth called the NS-Mesh) where the equations described in Section 2 are solved. Since our interest lies in primary and secondary atomization, NS-Mesh lies at the edge of the bell and extends a few millimeters outside of it. NS-Mesh requires a well-defined electric potential field (ϕ) to obtain the electric field ($\mathbf{E}$). We solve for ϕ using appropriate BCs at the boundaries of NS-Mesh. However, Fig. 4(a) highlights that ϕ is well-defined (labeled Dirichlet) only at the nozzle (bell electric potential) and at the target surface (grounded) but is not readily available at the boundaries of NS-Mesh. Instead of assuming values of BCs on NS-Mesh, a new domain called e-Mesh that spans between regions of well-defined ϕ is initialized and used to obtain accurate BCs on NS-Mesh. The volume of e-Mesh is about 8000 times larger than that of NS-Mesh, i.e., the region of interest in this project lies in about 0.0125% of the volume of e-Mesh. Making NS-Mesh this large would require significantly more computational resources to solve the fluid dynamics far from the bell edge. The breakup activity and charge transport within the liquid, which are the processes of interest in this work, are already completed within the NS-Mesh domain. To avoid solving hydrodynamics outside of NS-Mesh, we create e-Mesh - a domain spanning the entire region between the bell and the target surface - to be used exclusively as an electric potential solver. A Dirichlet BC of the value of the bell electric potential is imposed on the top boundary where the nozzle overlaps e-Mesh. A zero potential boundary condition is imposed on the bottom boundary which represents the target surface. Periodic BCs are imposed on the z^+ and z^- boundaries of e-Mesh and Neumann BCs are imposed on its remaining boundaries. The right boundary (x^+) was chosen in such a

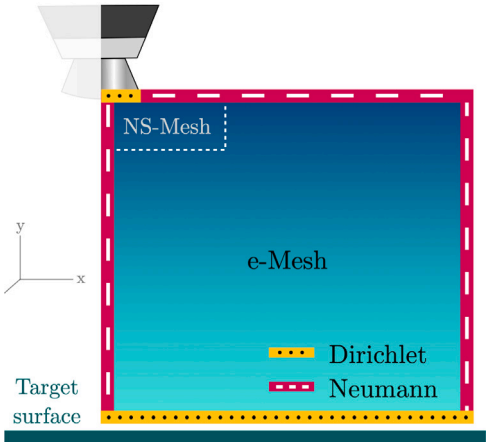

(a) e-Mesh shown in context with NS-Mesh and available ϕ BCs

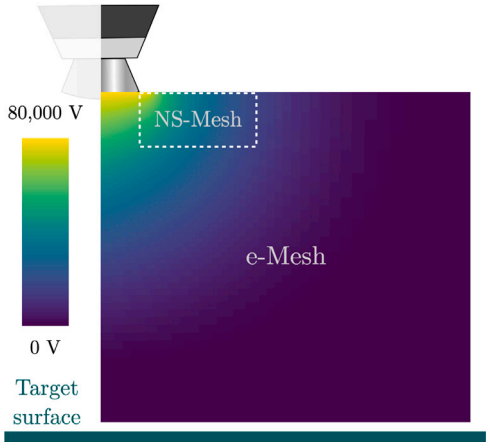

(b) Electric potential field (ϕ) on e-Mesh

Fig. 4. Boundary conditions and electric potential field (ϕ) on e-Mesh (not to scale)

way that it is far enough away that the electric potential field lines are perpendicular to the target surface, allowing for a Neumann BC to be imposed. In addition to the BCs, e-Mesh is populated with the charge density field (q) which is used to solve for ϕ (on e-Mesh) (Fig. 4(b)). Values of ϕ are interpolated from e-Mesh (which has a stretched grid and is coarser than NS-Mesh) to cells that lie on the boundaries of NS-Mesh using a tri-cubic interpolation method. These interpolated values are then used as BCs to compute ϕ on NS-Mesh.

3.3. Simulation setup

The domain geometry is represented schematically in Fig. 5. NS-Mesh, where the electrohydrodynamics is solved, has dimensions of 12.96 mm × 480 μm × 360 μm. e-Mesh, which spans from the bell edge to the target surface, has dimensions of 0.2 m × 0.25 m × 360 μm.

In this work, a bell of radius 25 mm is simulated. Some RBAs are equipped with serrations present at the edge of the bell which causes the fluid to be ejected as thin jets. In the absence of these serrations, the fluid forms liquid sheets on the inner surface of the bell. These liquid sheets may be subject to interfacial instability and form periodic ligaments at the edge of the bell or break up in sheet mode depending

Table 1
Standard values of parameters in the RBA simulations.

Property	Symbol	Value	Unit
Bell rotation rate	ω	40×10^3	RPM
Bell radius	R_{bell}	0.025	m
Edge angle	–	25	deg
Inlet jet diameter	D_{jet}	60×10^{-6}	m
Liq. flow rate	–	7.96×10^{-9}	m^3/s
Liq. viscosity	μ_l	0.1	Pa.s
Liq. density	ρ_l	1000	kg/m^3
Surface tension	γ	0.03	N/m
Bell electric potential	V_{bell}	80×10^3	V
Liq. charge density	q_l	2.879	C/m^3
Liq. rel. permittivity	κ_l	50	–
Liq. molecular diff.	$\mathcal{D}_l$	2×10^{-6}	m^2/s
Liq. ionic mobility	ψ_l	1.79×10^{-8}	$m^2/V\ s$

on the operating conditions. The bell simulated in this work is equipped with 418 serrations along its edge, each of which is 375 μm wide. While the liquid profile in a serration does not have a circular cross-section, we approximate a 60 μm diameter jet that exits the bell edge when operating at 40 kRPM (Domnick et al., 2005). For a nozzle flow rate of 200 mL/min, the flow rate through each serration is 7.96×10^{-9} m^3/s. In RBAs, the bell edge plane is angled away from the plane perpendicular to the axis of rotation. In the numerical setup, the jet is injected into the domain from the top wall with initial velocity components that correspond to an edge angle of 25° through an elliptical cross section. A magnitude of 2.879 C/m^3 for liquid charging is commonly applied to the liquid in industrial paint shops (Ellwood and Braslaw, 1998; Pendar and Páscoa, 2021). While the charging mode in practice does not typically yield a uniform bulk initial charge distribution, we assume such a case for simplicity. It is worth noting that the charges are still free to redistribute by the processes of advection, diffusion, and migration once the liquid is in the flow domain. In future work, the initial charge distribution in ligaments can be varied. Table 1 contains a list of parameter values used in simulations.

The top boundary is a wall that allows slip velocity and the left boundary is a no-flux wall. the bottom and right boundaries are convective outflows. Periodic BCs are imposed on the front and back walls. Although the periodic BCs on a Cartesian mesh would misrepresent jet interaction far from the bell edge, the angular separation of the jets close to the bell edge is not significant enough to account for its curvature. In addition to mass and momentum (and charge) being transported across the periodic z boundaries, the electric field is also computed with the effect of the periodicity. This means that at any instance the single jet simulated in the computational domain is solved with full consideration of its nearest neighboring jets.

The axis of rotation, which is the center of the bell, is located one radial length away (in the negative x direction) from the inflow. As mentioned previously, the model does not currently include a shaping air setup. Breakup is induced by imparting velocity modulations to the inflow. The inflow velocity ($\mathbf{u}_{\text{inflow}}$) is modulated by adding sinusoidal perturbations at a superposition of three (40, 50, and 60 kHz) frequencies ($\boldsymbol{\omega}$) at an amplitude (A) which is 9% of its original velocity ($\mathbf{u}$) (Eq. (18)).

$$\mathbf{u}_{\text{inflow}} = \mathbf{u} + \sum_{n=1}^{3} A \ \sin\left(2\pi\boldsymbol{\omega}_n t\right). \tag{18}$$

3.4. Mesh sensitivity

To determine the effect of mesh resolution on atomization and to help choose an optimal numerical setup, three simulations of an electrified RBA jet (Table 1) are performed with varying mesh resolutions (Table 2). We note from Fig. 6 that droplets larger than 10 μm are resolved in a 5 cells-per-diameter (CPD) mesh while the 10 CPD

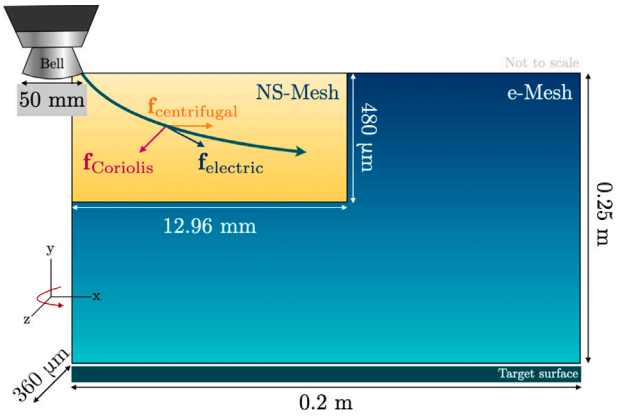

Fig. 5. A schematic representation of the domain geometry of the numerical problem showing positions and dimensions (not to scale) of NS-Mesh and e-Mesh.

Table 2
Mesh sensitivity simulation domain parameters.

Mesh ID	Cells per diameter	Cell width	Processor count	No. of structures
05 CPD	5	12 μm	16	74
10 CPD	10	6 μm	96	121
15 CPD	15	4 μm	256	705

mesh captures droplets smaller than 10 μm. Additionally, the 15 CPD mesh captures the droplets even smaller than 5 μm. Larger droplets are similarly resolved for all meshes. Between the two finer meshes the smaller droplets are increasingly well resolved.

We note the necessity for a mesh finer than 5 CPD since the coarseness of the mesh does not allow for charge migration to be captured. All liquid structures in the 5 CPD mesh contain the injected charge density value of 2.879 C/m^3. Using 10 and 15 CPD meshes, we are able to resolve the charge migration process and investigate the resulting droplet charge distribution. Most droplets contain a charge density close to the initial bulk charge density value. Compared to the initial charge density, it is more probable to find a droplet with a lower charge density. Fig. 7 highlights that charge migration is more resolved in a 15 CPD mesh and is consistent in its trend with the 10 CPD mesh. Although there is uncertainty with the smallest scales of droplet sizes, the number of droplets larger than 20 μm does not vary on increasing the mesh resolution, suggesting that the larger droplets are well resolved in a 15 CPD mesh. Since the goal of this project is to demonstrate the development of the tool, we believe that the underlying physical processes are sufficiently captured when using a 15 CPD mesh.

4. Results and discussion

Simulations are performed in a domain as described in Section 3.3 with parameters listed in Table 1.

4.1. Discussion of non-dimensional quantities

The non-dimensional numbers corresponding to the simulations are listed in Table 3. In the interest of understanding the effect of EHD on the flow, we present a brief discussion on the relevant non-dimensional numbers. The electric Reynolds number (Re_e) (Stuetzer, 1962) is the ratio of the charge advection timescale to the charge mobility timescale while the electric Péclet number (Pe_e) (Sheehy and Owkes, 2017) is a measure of the charge mobility timescale to the charge diffusion timescale. For high values of Re_e, charge migration is insignificant and the initial charge distribution will prevail in the liquid jet. For low values of Re_e, charge migration acts quickly to relax the charges to the surface allowing for surface charge models to be appropriate. For high values of Pe_e, charge migration dominates the charge diffusion process and vice versa. Based on the values of Re_e and Pe_e for this setup, it is reasonable to model all three charge dynamics processes, i.e., advection, diffusion, and migration, since their timescales are

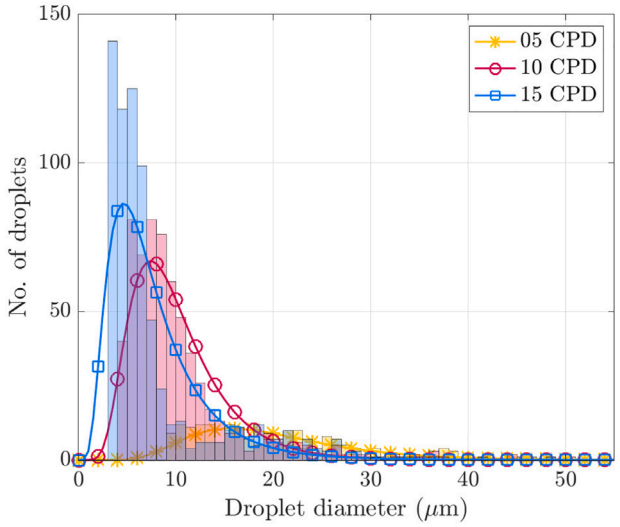

Fig. 6. Probability distribution of droplet sizes for varying mesh resolutions. The lines show a log-normal fit of the data.

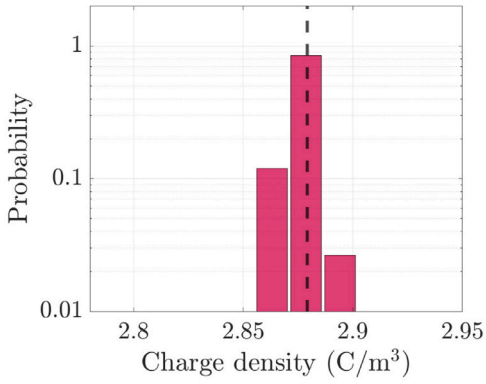

(a) 10 CPD

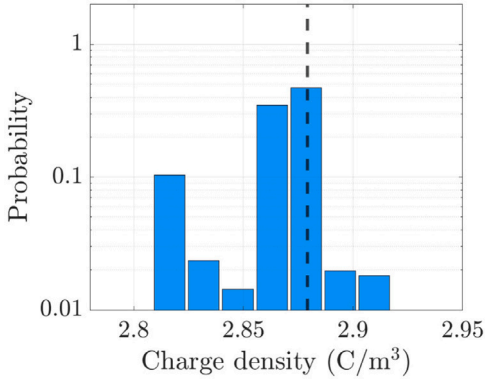

(b) 15 CPD

Fig. 7. Volume weighted charge density probability distributions for varying mesh resolutions. Note the logarithmic scale on the *y*-axis.

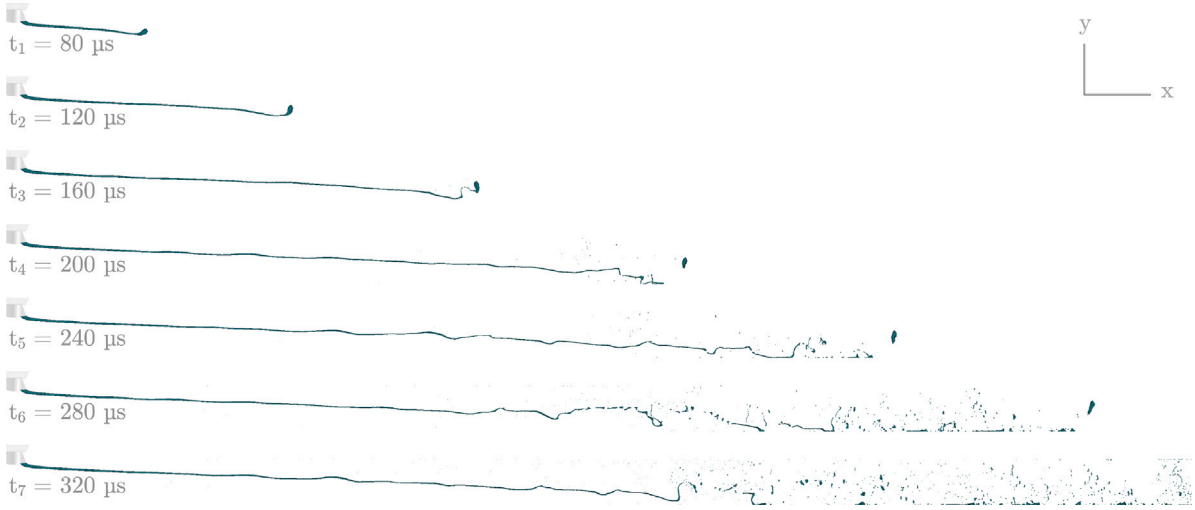

Fig. 8. Liquid interface positions of a single jet exiting the edge of the bell at different times as viewed from an x-y plane. The nozzle is shown for reference at the top left corner of each image and is not to scale.

Table 3
Non-dimensional numbers used in the RBA simulations.

Number	Definition	Value
Density ratio	ρ_l/ρ_g	830.56
Viscosity ratio	μ_l/μ_g	5546.31
Permittivity ratio	κ_l/κ_g	50.00
CFL	$\lvert\mathbf{u}_{\max}\rvert\Delta t/\Delta x$	0.30
Reynolds (Re)	$\rho_l\lvert\mathbf{u}_{\text{jet}}\rvert D_{\text{jet}}/\mu_l$	1006.24
Weber (We)	$\rho_l\lvert\mathbf{u}_{\text{jet}}\rvert^2 D_{\text{jet}}/\gamma$	77.87
Ohnesorge	$\sqrt{\text{We}}/\text{Re}$	0.0088
Electric Reynolds	$\epsilon_l\lvert\mathbf{u}_{\text{jet}}\rvert/(Lq_l\psi_l)$	8.93
Electric Péclet	$q_l\psi_l L^2/\left(D_l\epsilon_l\right)$	0.21
Electric Bond	$\epsilon_l\lvert E\rvert^2 L/\gamma$	0.091
Electro-inertial	$q_l^2 L^2/\left(\epsilon_l\rho_l\lvert\mathbf{u}_{\text{jet}}\rvert^2\right)$	0.0017

comparable to one another. The electric Bond number (Berthier and Brakke, 2012) quantifies the importance of the deforming electrical force compared to the restoring surface tension force. A low value signifies the dominance of surface tension-driven breakup activity. The electro-inertial number (Sheehy and Owkes, 2017) denotes the importance of EHD forces compared to inertial advective forces. A low value implies that inertial forces predominantly drive the hydrodynamics of the flow in this setup.

4.2. Electrified simulations of RBAs

Simulations of an electrified RBA jet in a 15 CPD mesh are performed with parameters listed in Table 1. Figs. 8 and 9 show the positions of the liquid interface of the jet at different instances in time as viewed from different viewing planes. We can capture complex and chaotic breakup activity comprising primary and secondary atomization that begins approximately 6 mm away from the bell edge. The breakup processes leading to primary atomization consist of ligament thinning, Rayleigh–Plateau instabilities and aerodynamic breakup due to interaction with quiescent air.

Primary atomization is first observed about 130 diameters downstream of the bell edge. Various parameters including the rotation rate, surface tension coefficient, and liquid viscosity affect the distance at which primary atomization begins. Additionally, the electric field has a complex effect due to a combination of its stabilizing effect in some applications and its impact on reducing the effective surface tension of the liquid. The effect of the electric field on breakup is discussed in more detail in Section 4.4. It is therefore worth exploring the physics of the breakup process in the future.

4.3. Parameter study

We conduct a parameter study on a 15 CPD mesh to investigate the impact of changing four parameters - nozzle rotation rate, nozzle flow rate, liquid charge density, and bell electric potential - one parameter at a time. Results of the parameter study are shown in Fig. 10 as snapshots of the liquid interface after 200 μ s. The values of all parameters are listed in Table 1 unless otherwise stated in the figure.

As the nozzle rotation rate increases, centrifugal forces are stronger on the jet and stretch it out faster leading to early elongation and breakup (Fig. 10(a)). Slower rotation rates do not stretch the jet out as much in the same duration. A higher flow rate through the same jet diameter acts in the same way as increasing jet velocity, which initially pushes the jet out further before centrifugal forces take over (Fig. 10(b)). While experimental studies are limited in their ability to independently vary the flow rate or rotation rate without affecting the jet diameter, the numerical model allows such tests to be performed.

An increase in either q_{in} or ϕ_{bell} stretches the jet along its downstream direction (Figs. 10(c), 10(d)). This is because the Coulomb force vectors point towards the direction of propagation of the liquid jet, i.e., the electric potential field contour lines are approximately perpendicular to the liquid velocity at that location. It is evident that no other significant effects of q_{in} or ϕ_{bell} are observed on the length of ligaments, as expected from the low value of the electro-inertial number.

4.4. Comparing electrified and non-electrified operation

In order to identify the effect of EHD on atomization, we compare a standard electrified jet (presented in Section 4.2) with a non-electrified jet. Numerical experiments of the latter are performed in a setup identical to that of the electrified simulation (Table 1) but with zero liquid charge density and zero bell electric potential.

In this particular simulation, after 300 μs, an electrified jet contains about 40% more droplets than a non-electrified jet. A lateral shift is

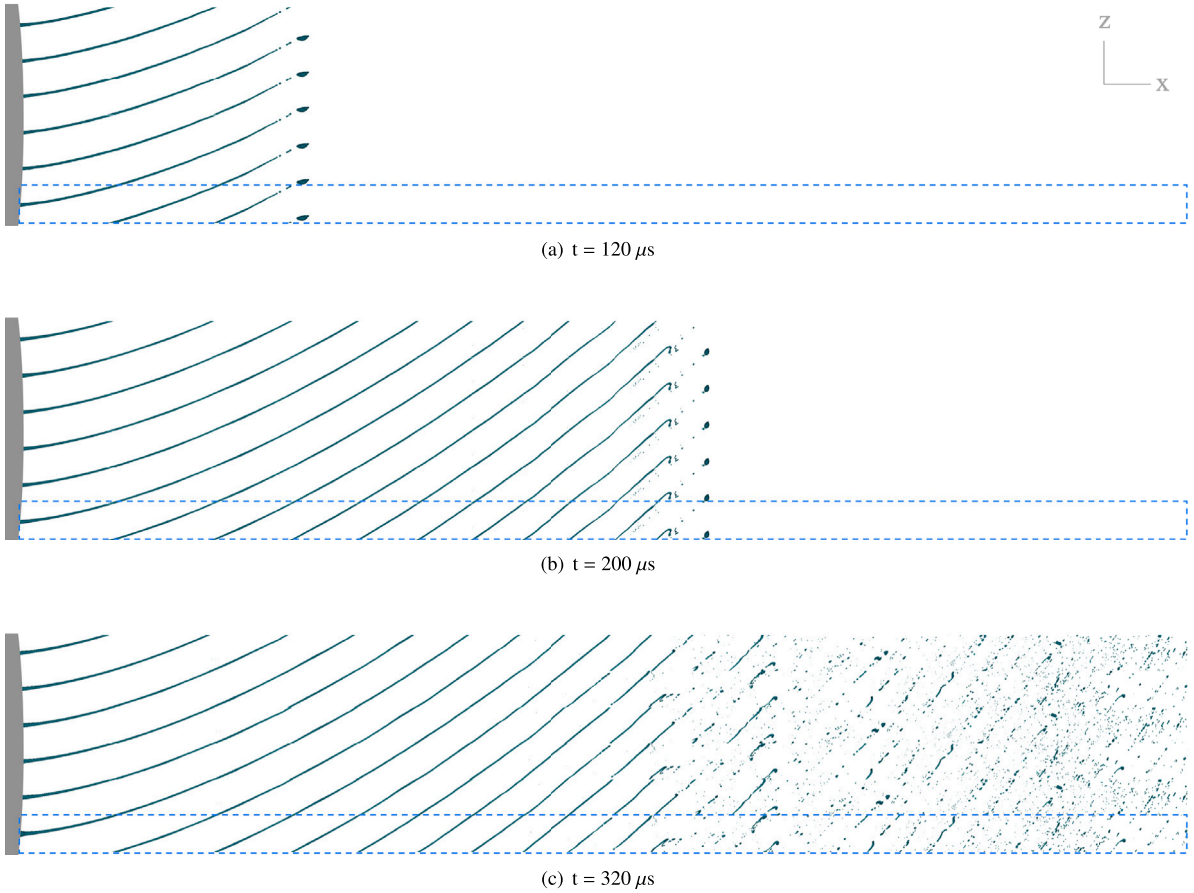

Fig. 9. Liquid interface positions of six individual jets exiting a serrated bell edge at different times as viewed from an $x-z$ plane. The nozzle is rotating clockwise and is shown for reference at the left edge of each image and is not to scale. The simulation domain is outlined by a dashed box. Owing to the periodic boundary conditions along the z-axis, an arc along the bell edge spanning six serrations is depicted in this view by stacking the domains in an attempt to vaguely recreate some experimental images available in Shirota et al. (2012), Oswald et al. (2019), Domnick (2010) and Wilson et al. (2018).

evident in the probability distribution of the size distribution between the two cases (Fig. 11(a)), i.e., the most probable diameter in an electrified jet is about 8% smaller than a non-electrified jet. Moreover, both the number and probability distributions show that significantly more droplets of smaller size are produced when the jet is electrified. This behavior is in agreement with the findings presented in Pendar and Páscoa (2021) where a similar shift towards smaller droplets has been observed in the number distribution for increasing background potentials. According to Pendar and Páscoa (2021), the presence of an electric field causes a net reduction in the effective surface tension in large droplets and ligaments and therefore an increase in the local Weber number of the structures. This can be the reason behind the increased rate of breakup and the production of smaller droplets in an electrified setup. Fig. 11(b) highlights that droplets are created at a higher rate in an electrified domain. The delay in the first instance of atomization in a charged jet is speculated to be due to a stabilizing force provided by the electric field on the liquid core (Bhuptani and Sathian, 2017; Saville, 1971; Nayyar and Murty, 1960; Saville, 1970; Mestel, 1996). However, once the breakup begins, the electric field accelerates the breakup process. This behavior will be further investigated in future work.

It is valuable to know the charge density in droplets after atomization. Fig. 12(a) shows that a majority of the droplets contain a charge density that is very close to the input charge density (shown as a black dashed line). Additionally, compared to the initial charge density, it is more probable to find a droplet with a lower charge density. This can be explained as follows - as charges relax and move to the surface of the ligament, the charge density in the bulk of the liquid reduces. Since a majority of the liquid structures break off the bulk volume (simply because of a greater liquid volume in the bulk than near the surface), most droplets contain a charge density slightly lower than the input value. The process of charge relaxation determines the distribution of charge in droplets. The electric Reynolds number listed in Table 3 is the ratio of the residence time of liquid in the domain to the charge relaxation timescale. The moderate value of 8.93 indicates that the charges have time to relax to some degree, but not enough time to fully relax to the surface. Furthermore, the computed electric Reynolds number is an overestimation of its true value as the velocity used to calculate the liquid advective timescale is at the bell edge - which is a significant underestimation. The velocity of the jet rapidly increases by about 30 times due to the centrifugal force. It is therefore possible that the charges do not fully relax through the ligament before atomization occurs. This is supported by the observation that most generated droplets contain a charge density close to the initial bulk charge value. Further studies are required to fully understand the relaxation of charges in the ligament and the factors influencing the distribution of charges in atomized droplets.

A common question in industrial applications is whether the droplets contain enough charge to overcome surface tension and undergo fissive breakup. Lord Rayleigh considered the balance of the

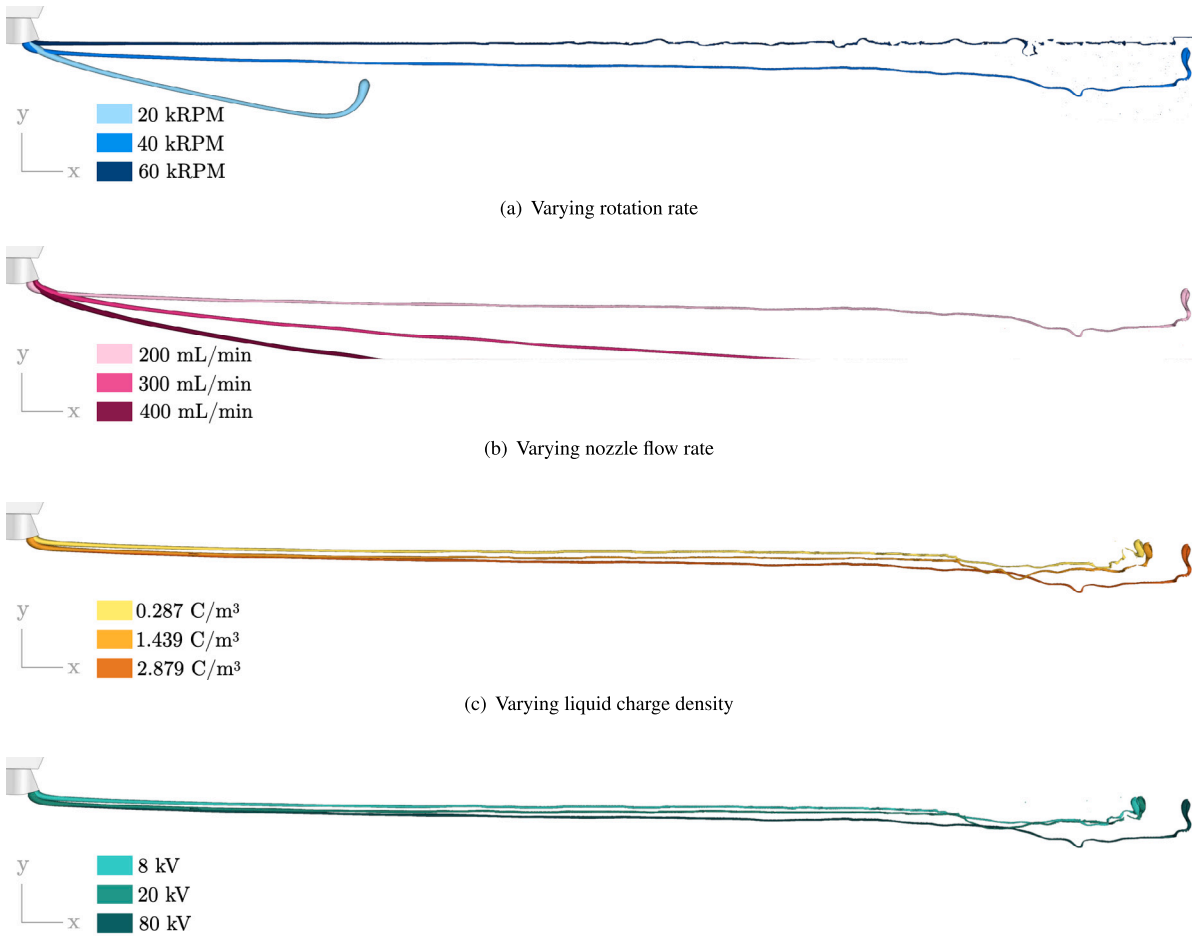

Fig. 10. A comparison of snapshots of the liquid interface positions after 200 μs in the parameter study simulations. The nozzle is shown for reference at the top left corner of each image and is not to scale.

destabilizing electrical force arising from the charges within a small droplet and the opposing capillary force due to its surface tension (Rayleigh, 1882). The result of this analysis based on the linear stability theory was the Rayleigh charge limit that defines the surface charge required to cause the fissive rupture of a charged droplet. Assumptions are often made regarding the charge contained in droplets after atomization (Domnick et al., 2005). We find that most droplets are charged to less than 5% of their corresponding Rayleigh limit (Fig. 12(b)). However, if the bulk charge density imparted to the liquid is increased, charge-driven Coulomb breakup might be observed.

The presence of charges in the liquid plays a role in the breakup process by causing more atomization. Electric charge can have an effect, albeit small, on primary atomization of ligaments and large droplets but a negligible effect on the size and stability of atomized droplets after secondary breakup. The feebleness of the electric field on atomization is further supported by the low value of the electric Bond number in the setup (Table 3). The effect of the electric charge on the droplet trajectories becomes significant at larger distances from the bell edge (Pendar and Páscoa, 2019; Im et al., 2004). However, small droplets are sometimes undesirable in the droplet cloud as they tend to disperse and escape as over-spray after atomization due to the weakness of the Coulomb force acting on them. Therefore, we believe that optimal operating conditions (electric field strength, liquid charge density, nozzle rotation rate, shaping air properties, liquid flow rate, etc.) that yield the highest TE and a suitable surface finish quality need to be determined carefully.

5. Conclusions

Electrostatic rotary bell atomizers are popular paint application devices used in the automotive industry. The charged setup that includes a background electric field increases the transfer efficiency of the device. In this work, we have built a tool to understand the effect of the electric field on near-bell droplet size and charge characteristics. This cost-effective method of simulating electrohydrodynamic atomization allows for the extraction of atomization statistics that are challenging to obtain experimentally in electrified setups.

A numerical model has been developed to simulate a liquid jet ejected from an electrostatic RBA. The formulation is built in a code called NGA that includes physics modules that accurately model EHD and a rotating frame. From the charge density distribution of atomized droplets, it is evident that most droplets contain a charge close to the initial bulk charge density value. Additionally, compared to the initial charge density, it is more probable to find a droplet with a lower charge density. Most droplets are charged to less than 5% of their corresponding Rayleigh limit suggesting that breakup is not primarily driven by fission due to charge accumulation. The presence of charges reduces the effective surface tension in large droplets and ligaments which leads

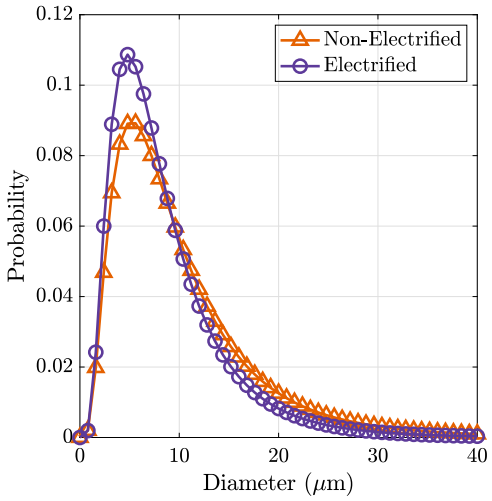

(a) Probability distribution of droplet sizes.

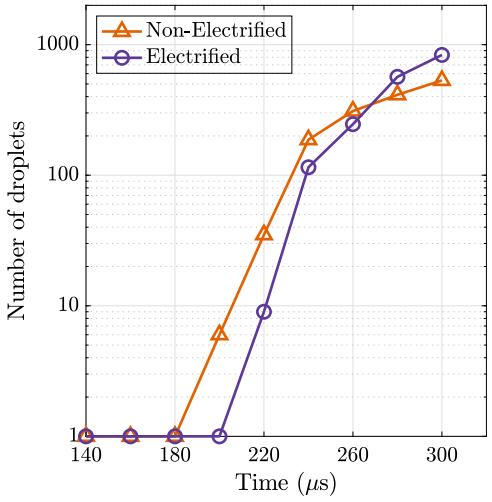

(b) Number of droplets in the domain. Note the logarithmic scale on the y-axis.

Fig. 11. A comparison of the atomization statistics between non-electrified and electrified simulations.

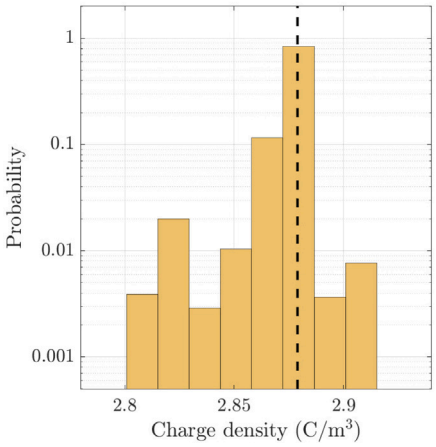

(a) Charge density probability distribution with the input bulk charge density shown as a black dashed line.

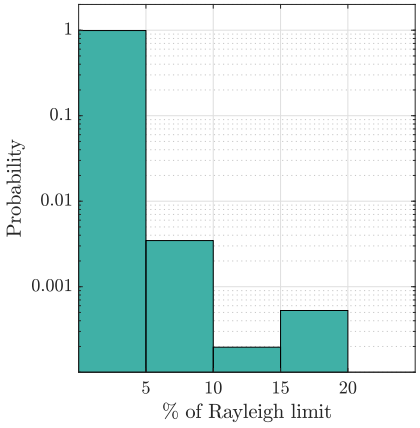

(b) Droplet charge density probabilities expressed in terms of their Rayleigh limit.

Fig. 12. Volume weighted charge density characteristics in atomized droplets. Note the logarithmic scales on the y-axes.

to the production of smaller droplets. If the charge density in the bulk liquid is increased, charge-driven Coulomb breakup might be observed. However, since smaller droplets tend to escape as over-spray, optimal operating conditions need to be determined carefully.

The tool developed can be employed to provide a set of initial conditions to a droplet cloud that includes information on position, diameter, velocity, and charge distributions to a flow solver that models the Lagrangian motion of droplets towards the target surface. In the future, this work will be extended to extract droplet genealogy statistics to identify the means of atomization in electrostatic RBAs. The simulation tool will also be used to conduct simulations on a finer mesh to understand the charge relaxation dynamics for non-uniform initial liquid charge distributions. A non-Newtonian model has been implemented into NGA and will be used to model the shear-thinning behavior of paint more accurately. Such development will allow for a deeper understanding of the charge distribution dynamics for industrial applications of RBAs.

CRediT authorship contribution statement

Venkata Krisshna: Writing – original draft, Methodology, Software, Validation, Formal analysis, Investigation, Visualization. **Wanjiao Liu:** Conceptualization, Writing – review & editing, Supervision. **Mark Owkes:** Conceptualization, Methodology, Software, Resources, Writing – review & editing, Supervision.

Declaration of competing interest

The authors declare the following financial interests/personal relationships which may be considered as potential competing interests: Mark Owkes reports financial support was provided by Ford Motor Company. Mark Owkes reports financial support was provided by National Science Foundation.

Data availability

No data was used for the research described in the article.

Acknowledgments

The project is supported and funded by the Ford Motor Company, United States. This material is based upon work supported by the

National Science Foundation, United States under Grant No. 1749779. The authors are grateful to Dr. Kevin Ellwood (Ford Motor Company) for many insightful discussions and guidance. The authors extend their gratitude to Dr. Erick Johnson, Dr. Yaofa Li, and Mr. Brendan Christensen for useful conversations and suggestions. Computational efforts were performed on the Hyalite High Performance Computing System and the Tempest High Performance Computing System, operated and supported by University Information Technology Research Cyberinfrastructure at Montana State University.

Appendix. Trajectory of an object influenced by the coriolis force

To validate the implementation of the Coriolis force in the flow solver, we performed a simulation of a liquid jet in a two-dimensional rotating frame and compared its trajectory to that provided by the analytical solution. Consider a point-like object of mass m at position $\boldsymbol{r}_0 = (x_0, y_0)$ moving with an initial velocity $\boldsymbol{v}_0 = (v_{x0}, v_{y0})$ in a frame rotating about the z axis with an angular velocity ω.

A force balance equation on the object influenced by centrifugal and Coriolis forces (14) can be formulated as

$$\boldsymbol{F} = m\boldsymbol{a} = -2\, m\boldsymbol{\omega} \times \boldsymbol{v} + m\boldsymbol{\omega} \times (\omega \times \boldsymbol{r})$$

where $\boldsymbol{a} = (\ddot{x}, \ddot{y})$ and $\boldsymbol{v} = (\dot{x}, \dot{y})$. On expanding the terms and separating the x and y components, we get

$$m(\ddot{x}\hat{x} + \ddot{y}\hat{y}) = 2\, m\omega\left[\dot{x}(-\hat{y}) + \dot{y}(\hat{x})\right] + m\left[\omega^2 x(\hat{x}) + \omega^2 y(\hat{y})\right].$$

We now separate the x and y components of the force balance equation to yield the following pair of coupled differential equations

$$m\ddot{x} = \; 2\, m\omega\dot{y} + m\omega^2 x$$
$$m\ddot{y} = -2\, m\omega\dot{x} + m\omega^2 y.$$

We now cancel out the mass terms and define $\eta = x + iy$. On adding i times the $\ddot{y}$ equation to the $\ddot{x}$ equation, we get

$$\ddot{x} + i\ddot{y} = \omega^2(x + iy) - 2i\omega(\dot{x} + i\dot{y})$$

which reduces to the form

$$\ddot{\eta} = \omega^2\eta - 2i\omega\dot{\eta}.$$

This linear second order differential equation has a solution of the form

$$\eta(t) = e^{-i\omega t}\left(C_1 + tC_2\right).$$

After imposing initial conditions of $\boldsymbol{r}_0$ and $\boldsymbol{v}_0$ and assuming $y_0 = 0$, we get $C_1 = x_0$ and $C_2 = v_{x0} + i(v_{y0} + \omega x_0)$. This gives the solution to η as

$$\eta(t) = x_0 e^{-i\omega t} + te^{-i\omega t}\left[v_{x0} + i(v_{y0} + \omega x_0)\right]$$

which can be decomposed to yield the x and y components of the object trajectory $\boldsymbol{r}$ by examining the real and imaginary parts as

$$x(t) = \left(x_0 + v_{x0}t\right)\cos(\omega t) + t\left(v_{y0} + \omega x_0\right)\sin(\omega t)$$
$$y(t) = -\left(x_0 + v_{x0}t\right)\sin(\omega t) + t\left(v_{y0} + \omega x_0\right)\cos(\omega t).$$

References

Ahmad, A.D., Singh, B.B., Doerre, M., Abubaker, A.M., Arabghahestani, M., Salaimeh, A.A., Akafuah, N.K., 2019. Spatial positioning and operating parameters of a rotary bell sprayer: 3D mapping of droplet size distributions. Fluids 4 (3).

Akafuah, N., Poozesh, S., Salaimeh, A., Patrick, G., Lawler, K., Saito, K., 2016. Evolution of the Automotive Body Coating Process — A Review. Coatings 6 (2).

Akafuah, N.K., Toda, K., Salazar, A., Saito, K., 2013. Automotive Paint Spray Characterization and Visualization. In: Automotive Painting Technology: A Monozukuri-Hitozukuri Perspective. Springer Netherlands, Dordrecht, pp. 121–165.

Anukiruthika, T., Moses, J., Anandharamakrishnan, C., 2021. Electrohydrodynamic drying of foods: Principle, applications, and prospects. J. Food Eng. 295, 110449.

Arumugham-Achari, A.K., Grifoll, J., Rosell-Llompart, J., 2015. A Comprehensive Framework for the Numerical Simulation of Evaporating Electrosprays. Aerosol Sci. Technol. 49 (6), 436–448.

Azizian, P., Azarmanesh, M., Dejam, M., Mohammadi, M., Shamsi, M., Sanati-Nezhad, A., Mohamad, A.A., 2019. Electrohydrodynamic formation of single and double emulsions for low interfacial tension multiphase systems within microfluidics. Chem. Eng. Sci. 195, 201–207.

Bailey, A.G., 1974. Electrostatic atomization of liquids. Sci. Progr.ss (1933-) 61 (244), 555–581.

Balachandran, W., Bailey, A.G., 1984. The Dispersion of Liquids Using Centrifugal and Electrostatic Forces. IEEE Trans. Ind. Appl. IA-20 (3), 682–686.

Berthier, J., Brakke, K.A., 2012. The Physics of Microdroplets. John Wiley & Sons.

Bhuptani, D.K., Sathian, S.P., 2017. Effect of axial electric field on the Rayleigh instability at small length scales. Phys. Rev. E 95 (5–1), 053115.

Blanquart, G., Pepiot-Desjardins, P., Pitsch, H., 2009. Chemical mechanism for high temperature combustion of engine relevant fuels with emphasis on soot precursors. Combust. Flame 156 (3), 588–607.

Chen, X., Cheng, J., Yin, X., 2003. Advances and applications of electrohydrodynamics. Chin. Sci. Bull. 48 (11), 1055–1063.

Clément, Z., Fredrik, E., Andreas, M., Oliver, H., 2014. Efficient Numerical Simulation of Spray Painting Processes in Automotive Manufacturing. In: 23rd SAE Brasil International Congress and Display. SAE Technical Paper.

Colbert, S.A., 2007. Numerical simulations of droplet trajectories from an electrostatic rotary-bell atomizer (Ph.D. thesis). Drexel University.

Colbert, S.A., Cairncross, R.A., 2005. A computer simulation for predicting electrostatic spray coating patterns. Powder Technol. 151, 77–86.

Corbeels, P.L., Senser, D.W., Lefebvre, A.H., 1992. Atomization Characteristics of a high speed rotary-bell paint applicator. Atom. Sprays 2 (2), 87–99.

Craig, I.P., Hewitt, A., Terry, H., 2014. Rotary atomiser design requirements for optimum pesticide application efficiency. Crop Protect. 66, 34–39.

Crowley, J.M., 1986. Fundamentals of Applied Electrostatics, vol. 1, first ed. Wiley.

Darwish Ahmad, A., Abubaker, A.M., Salaimeh, A.A., Akafuah, N.K., 2018. Schlieren Visualization of Shaping Air during Operation of an Electrostatic Rotary Bell Sprayer: Impact of Shaping Air on Droplet Atomization and Transport. Coatings 8 (8).

Desjardins, O., Blanquart, G., Balarac, G., Pitsch, H., 2008a. High order conservative finite difference scheme for variable density low mach number turbulent flows. J. Comput. Phys. 227, 7125–7159.

Desjardins, O., Moureau, V., Pitsch, H., 2008b. An accurate conservative level set/ghost fluid method for simulating turbulent atomization. J. Comput. Phys. 227, 8395–8416.

Dombrowski, N., Lloyd, T., 1974. Atomisation of liquids by spinning cups. Chem. Eng. J. 8 (1), 63–81.

Domnick, J., 2010. Effect of Bell Geometry in High-Speed Rotary Bell Atomization.

Domnick, J., Scheibe, A., Ye, Q., 2005. The Simulation of the Electrostatic Spray Painting Process with High-Speed Rotary Bell Atomizers. Part I: Direct Charging. Part. Part. Syst. Characterization 22 (2), 141–150.

Domnick, J., Thieme, M., 2006. Atomization Characteristics of High-Speed Rotary Bell Atomizers. Atom. Sprays 16 (8), 857–874.

Domnick, J., Yang, Z., Ye, Q., 2008. Simulation of the film formation at a high-speed rotary bell atomizer used in automotive spray painting processes.

Eagles, P.A.M., Qureshi, A.N., Jayasinghe, S.N., 2006. Electrohydrodynamic jetting of mouse neuronal cells. Biochem. J. 394 (2), 375–378.

Ellwood, K.R., Braslaw, J., 1998. A finite-element model for an electrostatic bell sprayer. J. Electrost. 45 (1), 1–23.

Ellwood, K.R., Tardiff, J.L., Alaie, S.M., 2014. A simplified analysis method for correlating rotary atomizer performance on droplet size and coating appearance. J. Coatings Technol. Res. 11 (3), 303–309.

Enayati, M., Chang, M.-W., Bragman, F., Edirisinghe, M., Stride, E., 2011. Electrohydrodynamic preparation of particles, capsules and bubbles for biomedical engineering applications. Colloids Surf. A 382 (1–3), 154–164.

Falgout, R.D., Jones, J.E., Yang, U.M., 2004. Pursuing Scalability for hypre's Conceptual Interfaces.

Falgout, R.D., Jones, J.E., Yang, U.M., 2006. The design and implementation of hypre, a library of parallel high performance preconditioners. In: Numerical Solution of Partial Differential Equations on Parallel Computers. Springer Berlin Heidelberg, pp. 267–294.

Farook, U., Stride, E., Edirisinghe, M.J., Moaleji, R., 2007. Microbubbling by co-axial electrohydrodynamic atomization. Med. Biol. Eng. Comput. 45 (8), 781–789.

Fredrich, D., Weiand, E., Giusti, A., 2022. Electrostatic fields for the control of evaporating charged fuel sprays. Int. J. Multiph. Flow. 104312.

Frost, A., 1981. Rotary atomization in the ligament formation mode. J. Agric. Eng. Res. 26, 63–78.

Fylladitakis, E.D., Theodoridis, M.P., Moronis, A.X., 2014. Review on the History, Research, and Applications of Electrohydrodynamics. IEEE Trans. Plasma Sci. 42 (2), 358–375.

Galitsky, C., Worrel, E., 2008. Energy Efficiency Improvement and Cost Saving Opportunities for the Vehicle Assembly Industry: An Energy Star Guide for Energy and Plant Managers. Technical Report, Lawrence Berkeley National Laboratory, University of California: Berkeley, CA, USA.

Geffen, C., Rothenberg, S., 2000. Suppliers and environmental innovation: the automotive paint process. Int. J. Oper. Product. Manag..

Gödeke, L., Oswald, W., Willenbacher, N., Ehrhard, P., 2021. Dimensional analysis of droplet size and ligament length during high-speed rotary bell atomization. J. Coatings Technol. Res. 18, 75–81.
Gorty, A.V., Barringer, S.A., 2011. Electrohydrodynamic spraying of chocolate. J. Food Process. Preserv. 35 (4), 542–549.
Grace, J., Marijnissen, J., 1994. A review of liquid atomization by electrical means. J. Aerosol Sci. 25 (6), 1005–1019.
Guettler, N., Knee, P., Ye, Q., Tiedje, O., 2020. Initial droplet conditions in numerical spray painting by electrostatic rotary bell sprayers: A framework for optimization of injection model coefficients. J. Coatings Technol. Res. 17 (5), 1091–1104.
Hayati, I., Bailey, A.I., Tadros, T.F., 1986. Mechanism of stable jet formation in electrohydrodynamic atomization. Nature 319 (6048), 41–43.
Hines, R., 1966. Electrostatic atomization and spray painting. J. Appl. Phys. 37, 2730–2736.
Hinze, J.O., Milborn, H., 1950. Atomization of Liquids by Means of a Rotating Cup. J. Appl. Mech. 17 (2), 145–153.
Im, K.-S., Lai, M.-C., Liu, Y., Sankagiri, N., Loch, T., Nivi, H., 2000. Visualization and Measurement of Automotive Electrostatic Rotary-Bell Paint Spray Transfer Processes. J. Fluids Eng. 123 (2), 237–245.
Im, K.-S., Lai, M.-C., Yoon, S.-J., 2003. Spray characteristics on the electrostatic rotating bell applicator. KSME Int. J. 17 (12), 2053–2065.
Im, K.-S., Lai, M.-C., Yu, S.-T.J., Matheson, R.R.J., 2004. Simulation of Spray Transfer Processes in Electrostatic Rotary Bell Sprayer. J. Fluids Eng. 126 (3), 449–456.
Jaworek, A., Sobczyk, A., Krupa, A., 2018. Electrospray application to powder production and surface coating. J. Aerosol Sci. 125, 57–92.
Kazama, S., 2003. Steady-state paint flow under high centrifugal force: atomization in spray painting. JSAE Rev. 24 (4), 489–494.
Keshavarz, B., Houze, E.C., Moore, J.R., Koerner, M.R., McKinley, G.H., 2020. Rotary atomization of newtonian and viscoelastic liquids. Phys. Rev. Fluids 5 (3).
Khan, M.K.I., Schutyser, M.A., Schron, K., Boom, R., 2012. The potential of electrospraying for hydrophobic film coating on foods. J. Food Eng. 108, 410–416.
Kourmatzis, A., Shrimpton, J.S., 2009. Electrohydrodynamics and charge injection atomizers: A review of the governing equations and turbulence. Atom. Sprays 19 (11), 1045–1063.
Kuhnhenn, M., Joensen, T.V., Reck, M., Roisman, I.V., Tropea, C., 2018. Study of the internal flow in a rotary atomizer and its influence on the properties of the resulting spray. Int. J. Multiph. Flow. 100, 30–40.
Laplace, P.-S., 2009. In: Somerville, M. (Ed.), Mechanism of the Heavens. In: Cambridge Library Collection - Physical Sciences, Cambridge University Press.
Leven, B., Weber, C., 2001. Energy efficiency in innovative industries: Application and benefits of energy indicators in the automobile industry. In: Proceedings ACEEE Summer Study on Energy Efficiency in Industry, vol. 1. pp. 67–75.
Loch, T., Nivi, H., Liu, Y., Lai, M.-C., Im, K.-S., 1998. An Experimental Investigation of Spray Transfer Processes in an Electrostatic Rotating Bell Applicator. In: International Body Engineering Conference & Exposition. SAE International.
Mackaplow, M.B., Zarraga, I.E., Morris, J.F., 2006. Rotary spray congealing of a suspension: Effect of disk speed and dispersed particle properties. J. Microencapsul. 23 (7), 793–809.
Mahmoud, A., Youssef, M.S., 2014. Influence of spinning cup and disk atomizer configurations on droplet size and velocity characteristics. Chem. Eng. Sci. 107, 149–157.
Makarytchev, S., Xue, E., Langrish, T., Prince, R., 1997. On modelling fluid flow over a rotating conical surface. Chem. Eng. Sci. 52 (6), 1055–1057.
Mark, A., Andersson, B., Tafuri, S., Engstrom, K., Sorod, H., Edelvik, F., Carlson, J.S., 2013. Simulation OF electrostatic rotary bell spray painting in automotive paint shops. Atom. Sprays 23 (1), 25–45.
McCarthy, J.E., Senser, D.W., 2005. Specific charge measurements in electrostatic air sprays. Particul. Sci. Technol. 23 (1), 21–32.
Melcher, J.R., 1981. Continuum Electromechanics, vol. 2. MIT press Cambridge, MA.
Melcher, J.R., Taylor, G.I., 1969. Electrohydrodynamics: A Review of the Role of Interfacial Shear Stresses. Annu. Rev. Fluid Mech. 1 (1), 111–146.
Mestel, A.J., 1996. Electrohydrodynamic stability of a highly viscous jet. J. Fluid Mech. 312, 311–326.
Naoki, I., Takuro, I., Yu, N., Seiichiro, I., Yu, F., 2019. Numerical simulation of droplet-formation in rotary atomizer. Theor. Appl. Mech. Lett. 9, 202–205.
Nayyar, N.K., Murty, G.S., 1960. The stability of a dielectric liquid jet in the presence of a longitudinal electric field. Proc. Phys. Soc. 75 (3), 369–373.
Ogasawara, S., Daikoku, M., Shirota, M., Inamura, T., Saito, Y., Yasumura, K., Shoji, M., Aoki, H., Miura, T., 2010. Liquid Atomization Using a Rotary Bell Cup Atomizer. J. Fluid Sci. Technol. 5, 464–474.
OICA, 2019. World Motor Vehicle Production - 2019 Production Statistics. Technical Report, Organisation Internationale des Constructeurs d'Automobiles.
Oswald, W., Lauk, J., Gödeke, L., Ehrhard, P., Willenbacher, N., 2019. Analysis of paint flow pulsations during high-speed rotary bell atomization. Coatings 9 (10), 1–9.
Owkes, M., Cauble, E., Senecal, J., Currie, R.A., 2018. Importance of curvature evaluation scale for predictive simulations of dynamic gas–liquid interfaces. J. Comput. Phys. 365, 37–55.
Owkes, M., Desjardins, O., 2014. A computational framework for conservative, three-dimensional, unsplit, geometric transport with application to the volume-of-fluid (VOF) method. J. Comput. Phys. 270, 587–612.
Owkes, M., Desjardins, O., 2015a. Consistent and conservative framework for incompressible multiphase flow simulations. In: APS Division of Fluid Dynamics Meeting Abstracts. pp. H7–007.
Owkes, M., Desjardins, O., 2015b. A mesh-decoupled height function method for computing interface curvature. J. Comput. Phys. 281, 285–300.
Owkes, M., Desjardins, O., 2017. A mass and momentum conserving unsplit semi-Lagrangian framework for simulating multiphase flows. J. Comput. Phys. 332, 21–46.
Oxley, J., 2012. Spray cooling and spray chilling for food ingredient and nutraceutical encapsulation. In: Encapsulation Technologies and Delivery Systems for Food Ingredients and Nutraceuticals. Elsevier, pp. 110–130.
Panneton, B., 2002. Geometry and Performance of a Rotary Cup Atomizer. Appl. Eng. Agric. 18 (4), 435–441.
Pendar, M.R., Páscoa, J.C., 2019. Numerical modeling of electrostatic spray painting transfer processes in rotary bell cup for automotive painting. Int. J. Heat Fluid Flow 80, 108499.
Pendar, M.R., Páscoa, J.C., 2020. Atomization and spray characteristics around an ERBS using various operational models and conditions: numerical investigation. Int. J. Heat Mass Transfer 161.
Pendar, M.-R., Páscoa, J.C., 2021. Numerical analysis of charged droplets size distribution in the electrostatic coating process: Effect of different operational conditions. Phys. Fluids 33 (3), 033317.
Precedence Research, 2019. Automotive Paints & Coatings Market Growth, Report 2020–2027 Automotive. Technical Report, Precedence Research.
Raje, P., Murmu, N.C., 2014. A Review on Electrohydrodynamic-inkjet Printing Technology.
Ray, R., Henshaw, P., 2018. Evaporation of clearcoat solvents from a rotary bell atomizer and its relationship with bell speed, flow rate, and electrostatic potential. J. Coatings Technol. Res. 15, 41–49.
Rayleigh, L., 1882. On the equilibrium of liquid conducting masses charged with electricity . London Edinburgh Dublin Philosoph. Mag. J. Sci. 14 (87), 184–186.
Rezayat, S., Farshchi, M., 2019. Spray formation by a rotary atomizer operating in the coriolis-induced stream-mode injection. Atom. Sprays 29 (10), 937–963.
Sadegh, P., Nelson, A., Kozo, S., 2018. Effects of automotive paint spray technology on the paint transfer efficiency – a review. Proc. Inst. Mech. Eng. D 232 (2), 282–301.
Saville, D.A., 1970. Electrohydrodynamic Stability: Fluid Cylinders in Longitudinal Electric Fields. Phys. Fluids 13 (12), 2987–2994.
Saville, D.A., 1971. Stability of Electrically Charged Viscous Cylinders. Phys. Fluids 14 (6), 1095–1099.
Saville, D.A., 1997. Electrohydrodynamics: The Taylor-Melcher Leaky Dielectric Model. Annu. Rev. Fluid Mech. 29 (1), 27–64.
Saye, R.I., Sethian, J.A., Petrouskie, B., Zatorsky, A., Lu, X., Rock, R., 2023. Insights from high-fidelity modeling of industrial rotary bell atomization. Proc. Natl. Acad. Sci. 120 (4), e2216709120.
Sheehy, P., Owkes, M., 2017. Numerical study of electric Reynolds number on electrohydrodynamic assisted atomization. Atom. Sprays 27 (7), 645–664.
Shen, B., Ye, Q., Guettler, N., Tiedje, O., Domnick, J., 2019. Primary breakup of a non-Newtonian liquid using a high-speed rotary bell atomizer for spray-painting processes. J. Coatings Technol. Res. 16, 1581–1596.
Shirota, M., Hatayama, Y., Haneda, T., Inamura, T., Daikoku, M., Saito, Y., Aoki, H., 2012. Formation and breakup of ligaments from a rotary bell cup atomizer.
Shrimpton, J.S., Laoonual, Y., 2006. Dynamics of electrically charged transient evaporating sprays. Internat. J. Numer. Methods Engrg. 67 (8), 1063–1081.
Sidawi, K., Moroz, P., Chandra, S., 2021a. Bell-cup serrations and their effect on atomization in electrostatic rotating bell atomizers. Exp. Fluids 62 (8), 1–16.
Sidawi, K., Moroz, P., Chandra, S., 2021b. On surface area coverage by an electrostatic rotating bell atomizer. J. Coatings Technol. Res. 18, 649–663.
Stevenin, C., Bereaux, Y., Charmeau, J.Y., Balcaen, J., 2015. Shaping Air Flow Characteristics of a High-Speed Rotary-Bell Sprayer for Automotive Painting Processes. J. Fluids Eng. Trans. ASME 137 (11), 1–8.
Stimpson, B.P., Evans Jr., C.A., 1978. Electrohydrodynamic ionization mass spectrometry of biochemical materials. Biomed. Mass Spectrom. 5 (1), 52–63.
Stuetzer, O.M., 1962. Magnetohydrodynamics and electrohydrodynamics. Phys. Fluids 5 (5), 534–544.
Symons, D.D., Bizard, A.F.M., 2015. Measurement of Fluid Flow Thickness Within a Rotating Cone. J. Fluids Eng. 137 (6).
Tatsuya, S., Tomoyuki, K., Junichi, T., Yasuhiro, S., Yohsuke, M., Hideyuki, A., Daichi, N., Genki, K., Masanari, M., Takukatsu, A., Masatoshi, D., Toshiki, H., Yohsuke, H., Minori, S., Takao, I., 2015. Liquid film flow on a high speed rotary bell-cup atomizer. Int. J. Multiph. Flow. 70, 96–103.
Taylor, G., 1966. Studies in Electrohydrodynamics. I. The Circulation Produced in a Drop by Electrical Field. Proc. R. Soc. Lond. Ser. A 291 (1425), 159–166.
Toljic, N., Adamiak, K., Castle, G.S., Kuo, H.H., Fan, H.T., 2011. Three-dimensional numerical studies on the effect of the particle charge to mass ratio distribution in the electrostatic coating process. J. Electrost. 69 (3), 189–194.
Turnbull, R., 1989. Self-acceleration of a charged jet. IEEE Trans. Ind. Appl. 25 (4), 699–704.
Vajdi Hokmabad, B., Faraji, S., Ghaznavi Dizajyekan, T., Sadri, B., Esmaeilzadeh, E., 2014. Electric field-assisted manipulation of liquid jet and emanated droplets. Int. J. Multiph. Flow. 65, 127–137.

Van Poppel, B., Desjardins, O., Daily, J.W., 2010. A ghost fluid, level set methodology for simulating multiphase electrohydrodynamic flows with application to liquid fuel injection. J. Comput. Phys. 229, 7977–7996.
Viti, V., Kulkarni, J., Watve, A., 2010. Computational fluid dynamics analysis of the electrostatic spray painting process with a rotating bell cup. Atom. Sprays 20 (1), 1–17.
Wang, X.T., Ning, Z., Lü, M., 2019. Linear instability of a charged non-Newtonian liquid jet under an axial electric field. J. Appl. Phys. 126 (13), 135301.
Wilson, J.E., Grib, S.W., Darwish Ahmad, A., Renfro, M.W., Adams, S.A., Salaimeh, A.A., 2018. Study of Near-Cup Droplet Breakup of an Automotive Electrostatic Rotary Bell (ESRB) Atomizer Using High-Speed Shadowgraph Imaging. Coatings 8 (5).
Yamamoto, T., Velkoff, H., 1981. Electrohydrodynamics in an electrostatic precipitator. J. Fluid Mech. 108, 1–18.